Title

Fundamental Studies of the Mechanism of Catalytic Reactions with Catalysts Effective in the Gasification of Carbon Solids and the Oxidative Coupling of Methane; Quarterly Report; April 1-June 30, 1994

Authors

Iglesia, E.
Perry, Dale L.
Heinemann, H.

Publication Date

1994-06-01

LBL-35876
UC-109

Center for Advanced Materials

CAM

Fundamental Studies of the Mechanism of Catalytic Reactions with Catalyst Effective in the Gasification of Carbon Solids and the Oxidative Coupling of Methane

Quarterly Report

April 1–June 30, 1994

E. Iglesia, D.L. Perry, and H. Heinemann

June 1994

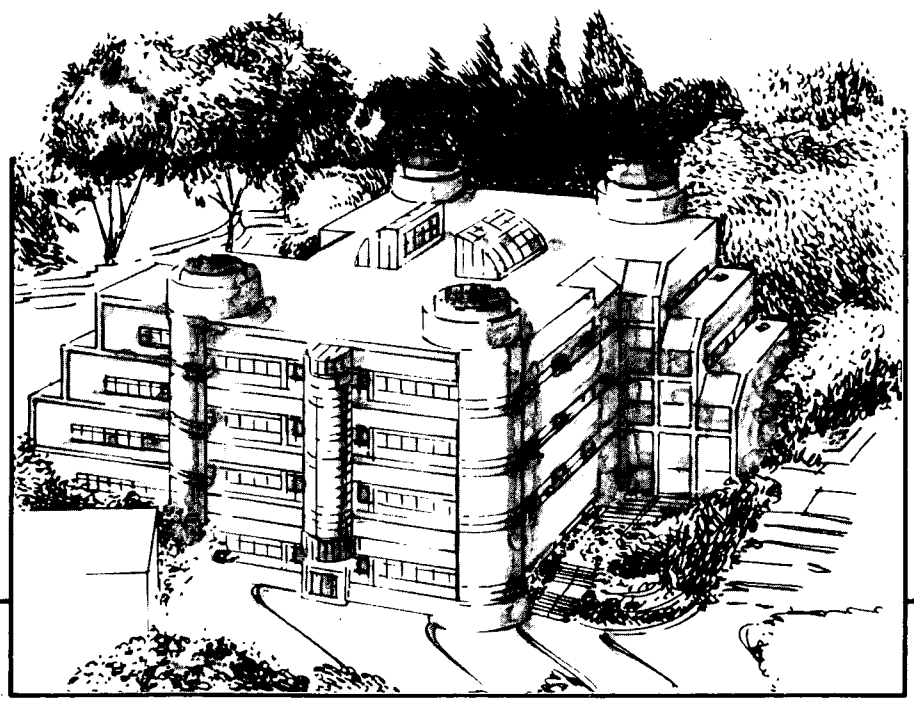

Materials and Chemical Sciences Division

Lawrence Berkeley Laboratory • University of California

ONE CYCLOTRON ROAD, BERKELEY, CA 94720 • (415) 486-4755

Prepared for the U.S. Department of Energy under Contract DE-AC03-76SF00098

DISCLAIMER

QUARTERLY REPORT

April 1, 1994 to June 30, 1994

FUNDAMENTAL STUDIES OF THE MECHANISM OF CATALYTIC REACTIONS WITH CATALYSTS EFFECTIVE IN THE GASIFICATION OF CARBON SOLIDS AND THE OXIDATIVE COUPLING OF METHANE

Principal Investigators: Enrique Iglesia
Dale L. Perry
Heinz Heinemann

Center for Advanced Materials
Materials Science Division
Lawrence Berkeley Laboratory
University of California
Berkeley, CA 94720

This work was supported by the Assistant Secretary for Fossil Energy, Office of Technical Coordination, U.S. Department of Energy under Contract DE-AC03-76SF00098, through the Morgantown Energy Technology Center, Morgantown, West Virginia 26505.

TABLE OF CONTENTS

ATTACHMENT: Slides: Presentation by H. Heinemann at Fossil Energy/National Laboratory Joint Meeting, "Catalytic Natural Gas Conversion Research", Dulles Airport Marriott, June 21, 1994.

I. Task Description for FY 1994

Task 1 - *Catalytic Steam Gasification of Coals and Cokes*: Work on the catalytic steam gasification of coals, chars, and petroleum coke will be phased out in 1994. Experimental work will be limited to a better understanding of the reaction of carbonaceous materials with steam in the presence of alkali introduced with the steam. A final report will be written, which will cover more than six years of research results.

Task 2 - *Oxidative Methane Coupling:* The CRADA between LBL and Orion ACT resulted in appreciable work and significant progress during FY1993. The positive effect of steam was recently shown to be a general phenomenon that applied not only to Ca-Ni-K oxides but also to several other widely studied oxidative coupling catalysts. Additional increases in ethylene and ethane yields will be pursued through the use of membrane and cyclic reactors. A membrane reactor has been constructed and proton-transfer membranes will be synthesized and tested in the oxidative coupling reactions. A unit is being redesigned to permit the testing of catalytic materials under cyclic conditions, in which methane is sequentially decomposed and the reaction products scavenged by O_2, H_2, or hydrocarbons. Detailed fundamental models of chemical reactions and of reactor hydrodynamics in cyclic and membrane reactors will be developed and used in the design of concept demonstration tests.

Task 3 - *Synthesis and Characterization of Catalysts*: Detailed spectrographic and wet chemical analyses of fresh and spent catalysts have shown significant differences, which have permitted conclusions as to the sources of deactivation; this work will continue in FY 1994. In addition, pulsed laser deposition techniques have shown the ability to form stoichiometric mixed metals oxides; this technique will be exploited in the synthesis of catalytic materials and thin film membranes.

II. Introduction

Catalytic gasification work has been completed and no other work is planned in the general area of catalytic gasification of coals and chars. A graduate student has completed his training in the operation of the membrane reactors and began experimental and theoretical studies of membrane reactors for the selective activation of methane. Task 2

has operated without a post-doctoral fellow because of budget limitations during the first two quarters of FY1994. Dr. S. Sundararajan joined the group in April 1994 and will be assigned to the project throughout the remaining of the fiscal year. He is an expert in the synthesis of thin metal oxide films for membrane and catalytic applications. Budgetary constraints have slowed down the re-design and start-up of the cyclic reactor unit (CRU). The unit is now operational but we have concentrated on the synthesis and characterization of membrane and catalytic materials during the present quarter.

III. Highlights

Our strategy for the selective activation of methane was described in a recent presentation by H. Heinemann at the Fossil Energy/National Laboratory Joint Meeting, "Catalytic Natural Gas Conversion Research", Dulles Airport Marriott, June 21, 1994. A copy of the slides used is included as an Attachment to this Quarterly Report.

a) Catalytic Steam Gasification of Coals and Cokes

A final report was written and forwarded to Mr. Rodney Malone, Project Manager, Morgantown Energy Technology Center during 2Q'1994. This requested final report completed our activities in coal gasification for FY1994. No further studies are planned.

b) Oxidative Methane Coupling

- Results published by Hamakawa, *et al.* in *The Journal of the Electrochemical Society* have confirmed the concept of methane coupling via a membrane reactor. These findings confirm our previous conclusion that thinner membranes and increased surface activity for C-H bond activation at low temperatures are required in order to reach commercially attractive rates of reaction.

- The initial analysis of a theoretical model comparing the membrane and cyclic processes has been completed. The results indicate that perovskite membranes on the order of 50 microns will be needed for the membrane operation to be superior to a cyclic one.

- Two techniques, laser ablation and spin-coating / sol-gel chemistry are being tried to prepare the thin membranes described above.

- X-ray diffraction (XRD) and scanning electron microscopy (SEM) analyses have been performed on thick (1 millimeter) membrane disks. These disks are being used in our membrane reactor to attempt reproduction of the data reported by Hamakawa, *et al.*

- A manuscript describing the results of our theoretical investigation into the gas phase and surface-catalyzed reactions of oxidative coupling is being submitted to *Chemical Engineering Science*.

c) Synthesis and Characterization of Catalysts

- Studies of the magnetochemical properties of the calcium-nickel-potassium oxide powdered catalysts have been concluded and a manuscript describing the work has been completed.

- Synchrotron x-ray fluorescence microprobe data for calcium-nickel-potassium films have been analyzed and an abstract of the results has been submitted for presentation at the Fall Meeting of the Materials Research Society.

- Initial films of strontium-zirconium oxide, using yttria-stabilized zirconia as a buffer layer, have been fabricated using pulsed laser deposition.

- X-ray diffraction data have been obtained for several of the strontium-zirconium-yttrium oxide films.

IV. Progress of Studies

a) Catalytic Steam Gasification of Coals, Chars, and Cokes.

The final report on this task has been completed and issued. No further work is planned in this area because of termination of financial support.

b) Oxidative Coupling of Methane

Verification of Membrane Concept

Recent work by Hamakawa, *et al.* has demonstrated the concept of using a membrane reactor for methane coupling with a ceramic membrane of composition $SrCe_{0.95}Yb_{0.05}O_{2.95}$ and a thickness of 1 millimeter in an electrochemical cell. A schematic of their design is shown in Figure 1.

At 900 °C, with no applied voltage, the formation of ethylene and ethane products was detected on the methane side of the membrane. Furthermore, by alternating argon or air on the hydrogen removal side, the C_2-formation rates increased three-fold. These results are shown in Figure 2. The increased formation rate is due to an increased chemical potential gradient across the membrane. By using air to form water on one side, the hydrogen potential of that side is reduced substantially. The larger potential gradient raises the rate of hydrogen diffusion through the membrane, and thus increases the overall rate of methane coupling.

Figure 1: Methane coupling to C_2 compounds using $SrCe_{0.95}Yb_{0.05}O_{2.95}$ as a solid electrolyte.

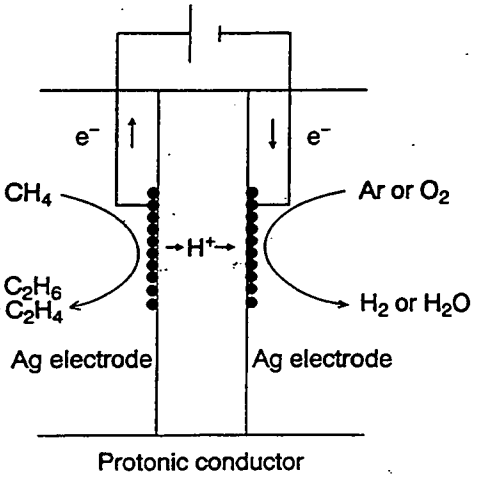

Figure 2: Changes in C_2 formation rate with argon and air streams opposite from methane side of membrane.

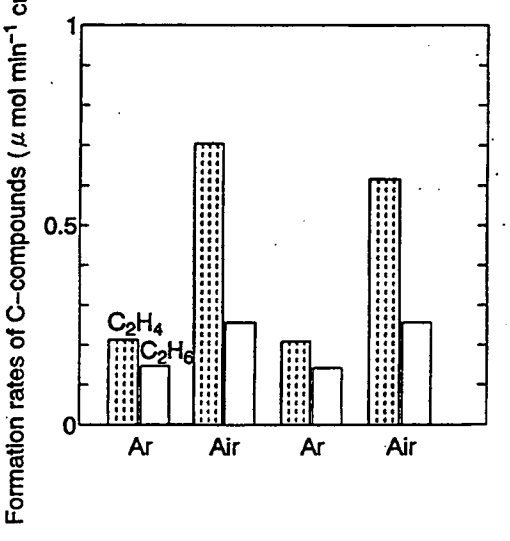

Hamakawa, S., Hibino, T., Iwahara, H., *J. Electrochem. Soc.*, 140, 2, February 1993.

The reported C_2-formation rates are very low and the high temperatures required are too high for this specific system to be attractive for practical applications. Also, the use of silver electrodes in this cell lead to a coke formation rate four times that of the C_2-compounds. However, the results prove the concept of using a hydrogen transport membrane to form C_2 products from methane. As predicted, the product was free of CO_x species that limit the yields attainable in conventional processes. The technical hurdles identified by this study are: i) fabrication of thinner membranes (<0.1 millimeter) of stoichiometric perovskite composition; ii) higher rates of methane activation on the methane side of the membrane films by control of surface coating or films; iii) higher rates of hydrogen removal at the oxygen side of the membrane. We previously identified these hurdles based on theoretical considerations and our experimental program specifically attempts to overcome these hurdles to the efficient application of hydrogen transport membranes in methane and higher alkane activation processes.

Time-Space Relationships in Cyclic and Membrane Reactors

We have developed a rigorous mathematical comparison of the maximum hydrogen throughput available in the transient (cyclic) and membrane reactors. In a steady-state process, the hydrogen removal rate from methane is directly related to the formation rate of C_2 species. Figure 3 is a diagram of the two models used.

An analytical solution has been found for the case of semi-infinite slabs and diffusion-limited kinetics. Non-dimensionalized variables were used in the analysis, in order to make the solution independent of the type of material used for the membrane. The solution to these models demonstrates a direct mathematical relationship for the maximum possible rate of hydrogen transport using the two types of reactors. Figure 4 shows this result.

Figure 4 can be used as a guide to selecting which reactor scheme is best to use for a given hydrogen transport material. From the graph, it can be seen that for a dimensionless cycle time (τ) less than 1.0, the cyclic reactor mode has higher product throughput than the membrane reactor. Therefore, optimum designs of membrane reactors must include an inorganic solid with high proton diffusivity and significant mechanical and structural integrity as a thin disk.

Figure 3: Reactor Models

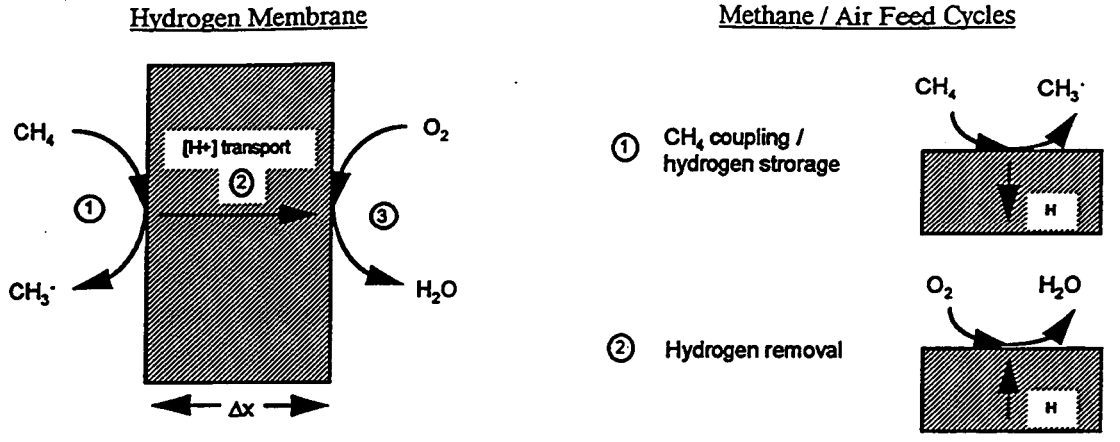

Figure 4: Membrane to Cyclic Hydrogen Flux Ratio versus Material Properties.

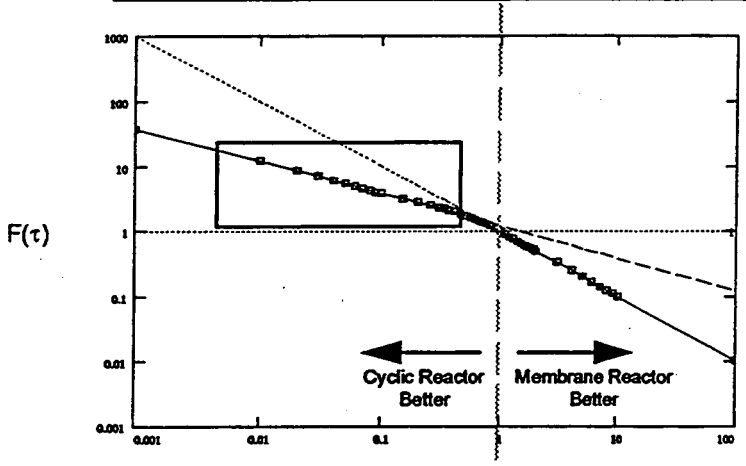

$$F(\tau) = \frac{J_{cyclic}}{J_{membrane}}$$

$$\tau = \frac{t \cdot D_H}{\Delta x^2}$$ *(Dimensionless cycle time)*

J_{cyclic} = Total hydrogen flux through cyclic operation
$J_{membrane}$ = Total hydrogen flux through membrane operation
t = Length of feed cycle in cyclic operation
D_H = Diffusion coefficient of hydrogen in conducting / storage material
Dx = Thickness of membrane in membrane operation

squares - calculated points **bold line** - fitted curve **dashed lines** - asymptotes
box - range currently achievable with perovskite membranes

For example, with the $SrCe_{0.9}Y_{0.1}O_{2.95}$ membrane currently under study, the approximate parameters are a cycle length (τ) of 10 seconds, a thickness (Δx) of 0.5 millimeter, and a hydrogen diffusivity (D_H) of 10^{-4} cm^2/s. This is equivalent to a dimensionless cycle time of 0.4. From Figure 4, it is seen that cyclic operation provides a larger product throughput for a membrane with this value of τ.

Synthesis and Characterization of Thin Membranes

The model described above demonstrates the need for thinner hydrogen membranes than those currently available. We are pursuing two techniques that will produce membrane films of thickness less than 50 microns. The first is vapor deposition of perovskite on a porous alumina substrate using a technique called laser ablation. This process uses a high-energy laser to vaporize a stoichiometric mixture of the desired material. The vapor deposits on an alumina disc, which provides mechanical support. The result is a uniform thin film with perovskite structure. The technique has worked successfully in the past for superconducting films of related composition and structure.

The second technique is spin-coating coupled with sol-gel synthesis. Both of these methods have been widely used in materials science for the preparation of uniform materials and thin films. Our plan is to spin a porous alumina disc or cylinder in a solution of perovskite precursors. Upon the addition of water, the sol-gel reaction will be initiated to drive the precursors into a uniform, hole-free structure. With proper adjustment of the rotational speed and reaction times, it is possible to form very thin films of the desired composition.

Synthesis, Characterization and Evaluation of Membrane Disks (1 mm thickness)

Concurrently with the efforts to produce thinner membranes of stoichiometric perovskite compositions, we continue our studies of high-temperature densification of perovskite powders under applied pressure in high-temperature dies. These pre-forms were successfully cut into disks of 0.5-1 mm thickness. The perovskite structures were maintained during the densification process. The x-ray diffraction pattern corresponds to a stoichiometric perovskite of composition $SrZr_{0.9}Y_{0.1}O_{2.95}$ (Figure 5a). Preforms with up to 94% of the theoretical solid density have been obtained, corresponding to about 6% void fraction. Theoretical models developed to describe the porous structure of such materials

are shown in Figure 6a. The rigorous description of these materials has shown that no percolating channels are expected to traverse macroscopic perovskite disks with less than about 8% void fraction. This is shown by the infinite tortuosity that is reached at porosities below 6% in Figure 6b.

Scanning electron micrographs show that the disks cut from the compressed pre-forms have relatively smooth surfaces and few cracks and imperfections (Figure 5b). Some shallow pits of less that 1 - 2 microns in depth are present on the surface but are not deep enough to traverse the membrane. SEM micrographs also show that scratch lines form on the disk surface during the cutting process. These scratch marks are very shallow and will not impact the permeability and selectivity of these membranes but may act as nucleation sites for the development of deeper cracks spanning the membrane thickness. Such cracks have plagued some of our previous attempts to use these materials at very high temperatures in methane conversion reactors. We plan to examine the role of these scratch marks in membrane failure and to modify the cutting procedures if they are found to be responsible for the high temperature failure of these disks during catalytic reactions at high temperatures.

Catalytic evaluation studies are being conducted following delays associated with the imperfect sealing of membranes in this reactor and with the move of the reactor unit from Building 66 in the Lawrence Berkeley Laboratory to Hildebrand Hall in the Berkeley Campus. This move was required in order to provide for a hood exhaust environment in which to carry out studies with oxygen-methane mixtures.

Theoretical Descriptions of Reaction-Separation Schemes

Oxidative coupling reactions occur by complex reaction networks involving both gas phase and surface-catalyzed reactions. The design and testing of reaction-separation concepts to avoid deleterious full oxidation of reactive C_2 products to CO_x requires the development of detailed models. We have recently completed the development of such models and we are beginning their use in a systematic study of the potential benefits of various proposed reaction-separation schemes. These models are essential in guiding our laboratory experiments using membrane and cyclic reactors and in the ultimate design of such reactors for industrial practice.

Figure 5a: X-ray diffraction pattern of perovskite disk

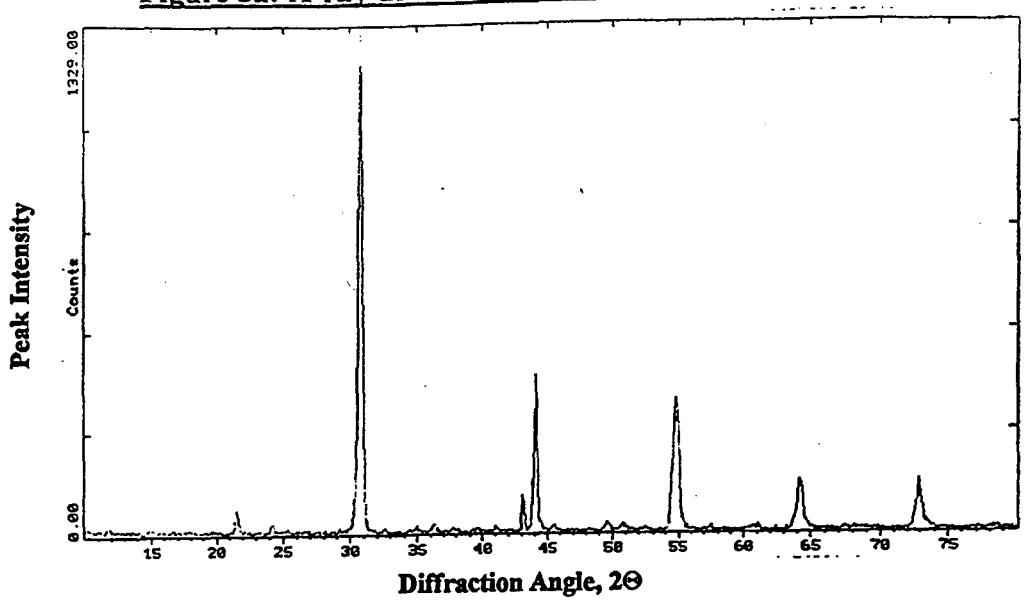

Figure 5b: Scanning electron micrograph of disk surface

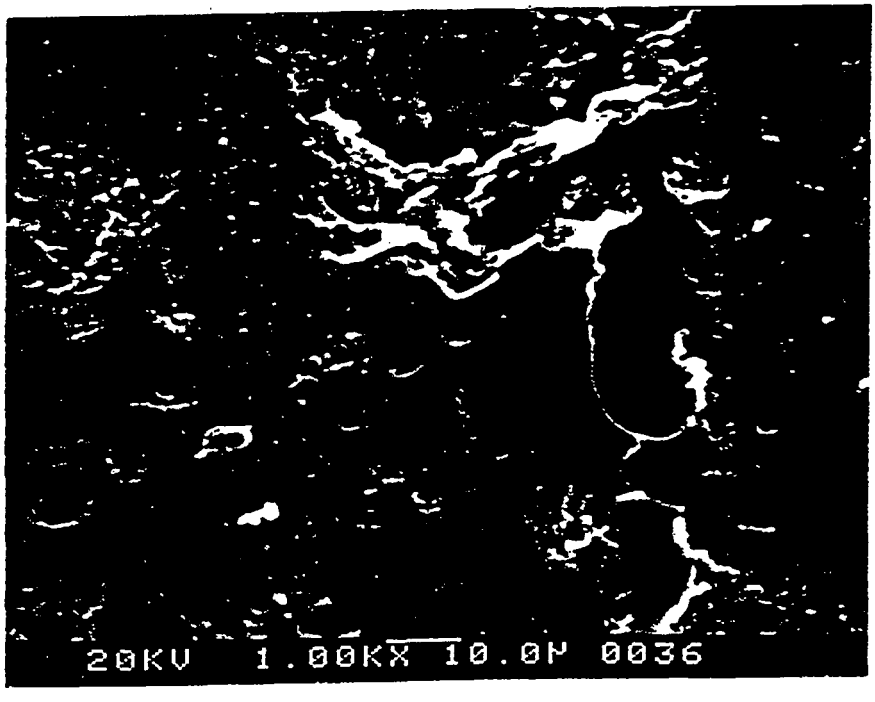

Inorganic composition of membrane was 50.5 wt% Zr, 41.1 wt% Sr, 8.2 wt% Y, 0.25 wt% Ca (impurity)

Figure 6a: Three-dimensional view of simulated sintered porous solid

Figure 6b: Tortuosity factors in simulated compressed and sintered porous solids

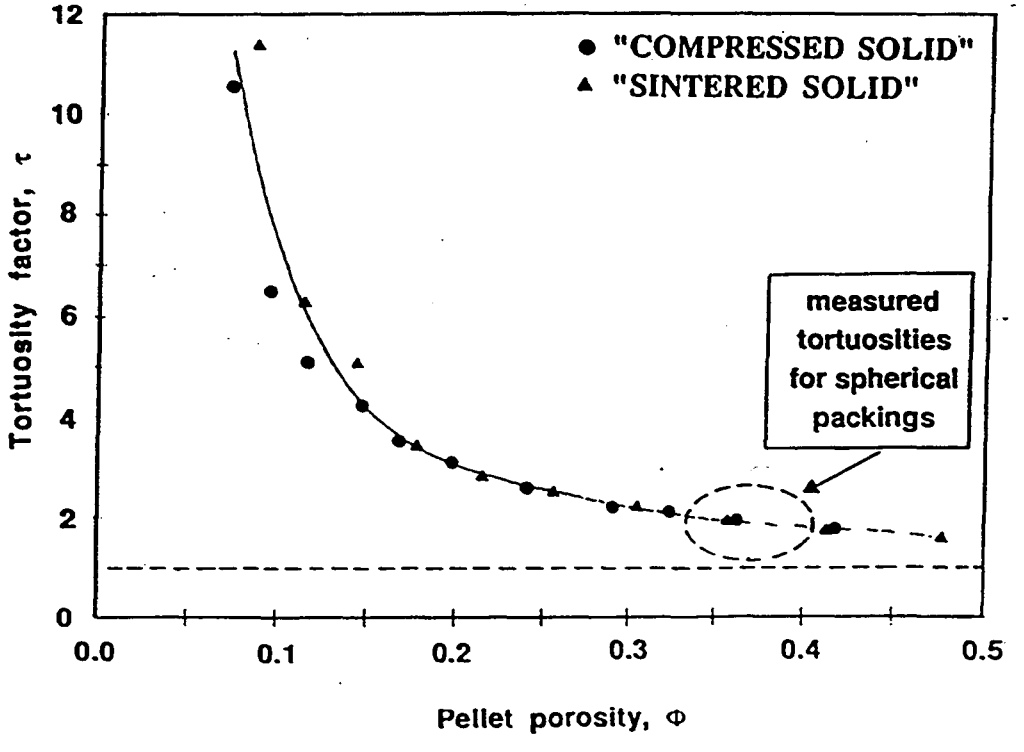

The detailed results of this research have been described in a manuscript that is being submitted to *Chemical Engineering Science*.

c) Synthesis and Characterization of Catalysts

Magnetochemical Studies on Powdered Calcium-Nickel-Potassium Catalysts

Several different samples prepared at various periods of heating and at different temperatures were chosen for magnetochemical investigation, the samples being prepared using the same reagents in each case. One sample was prepared without the potassium component so that the sample could act as a control having a constant composition. The change in composition with the potassium samples comes from the slow departure of potassium oxide species at lower temperatures relative to those of the calcium and nickel oxides. This sample also allowed a magnetochemical study of the nickel system without any possible synergism between the nickel and potassium oxides, so that the results would reflect on the chemical syntheses effects of the nickel chemical state.

The magnetic measurements were performed with a Quantum Design Model MPMS SQUID magnetometer. (SQUID is an acronym for Superconducting QUantum Interference Device). The static magnetic moment was measured over the temperature range 5 to 280 K and over the magnetic field range 0 to 40 kiloGauss (0 to 4 Tesla). The usual procedure was to determine the magnetic moment while warming the sample from 5 K to 280 K in a field of 10 kiloGauss, followed by cooling back to 5 K in a field of 40 kiloGauss and concluding by reducing the field from 40 kiloGauss to zero at 5 K. The time for each individual moment determination was about 30 seconds. A correction was made for the diamagnetic plastic sample container, based on its measured moment.

Samples A and B proved to be particularly magnetic, as shown in Figure 7. The markedly non-linear behavior of magnetic moment with field, saturating at fields below 10 kiloGauss, is suggestive of metallic nickel. The linear slope observed at the higher fields is attributed to the linear dependence of magnetization on field expected for antiferromagnetic NiO. The saturation moment decreases weakly with increasing temperature (not shown), which is also indicative of nickel. These results are in general agreement with prior work with powders containing fine nickel particles.[11,13] Based on the saturation moment of bulk nickel, the fraction of nickel which is present in the metallic

form is estimated as 1.5% for Sample A and 5% for Sample B. Since Samples A and B were prepared in identical fashion, except that B was doped with potassium, it appears that potassium assists the formation of Ni° in this case. The x-ray diffraction results shown in Figure 8 exhibit small peaks for nickel, at precisely the location (44.5°) of the most intense diffraction peak in the nickel spectrum, confirming the presence of metallic nickel.

The magnetic moment of the other four samples is shown in Figure 9 as a function of field. In each case the plot is more nearly linear for these less magnetic samples. Sample C, which was calcined at relatively low temperatures, has an anomalously high moment compared with the other Samples D, E, and F. This enhanced moment is attributed to the superparamagnetism of NiO particles smaller than 100 nanometers.[15,17-23] It is not seen in the other samples due to the higher processing temperature which promotes the growth of larger grains. The curvature in these plots is due to paramagnetic "impurities," possibly Ni^{3+} ions associated with excess oxygen, to be discussed below in connection with the temperature dependence at low temperatures. The large remnant moment of Sample C can be identified with the locking of the superparamagnetic moment below the blocking temperature.

Data at lower fields are shown for all six samples, in Figure 10. Note that the low-field behavior of the metal-containing Samples A and B is qualitatively different from that of the other samples, a fact which is useful in detection of Ni° in oxide mixtures. Sample C has the largest remnant moment, 0.055 emu per gram. If this remnant moment were due to nickel metal, the fraction of nickel in the metallic form would be roughly 0.3%, too small to be readily detected by x-ray diffraction. The more magnetic Samples A and B show rather small remnant moments (only a few percent of the saturation moments), even at 5 K. For superparamagnetic nickel particles, one may expect that the blocking temperature is above 5 K, and that therefore the remnant moment should be larger. For example, Gittleman et al.[10] give blocking temperatures of 20 K for 4 nanometer particles and show a trend toward smaller blocking temperatures for smaller particles. However, the existence of a sharp x-ray diffraction peak shows that some of the particles must be at least a few nanometers in size. To summarize, the remnant moments for Samples A and B show that most of the moment associated with elemental nickel is not aligned at 5 K and zero field, presumably due to thermal agitation. While this observation is puzzling, it is in agreement with prior observations on some samples with small nickel particles.[24]

Figure 11 shows the temperature dependence of the moment of NiO reagent powder and Samples C, D, and F. The data for NiO have been scaled as though the NiO had been diluted (3.04 : 1 by weight) by non-magnetic $Ca(OH)_2$, for comparison with the other samples. Table 2 gives numerical results at 280 K and 40 kiloGauss for all samples. The measurement for NiO corresponds to a magnetic susceptibility of 1.18×10^{-5} emu gm^{-1} Oe^{-1} at 280 K, which may be compared with 9 to 9.5×10^{-5} for larger particles of NiO and single crystals.[15,16,22] According to Richardson *et al.*,[22] the room temperature value of the susceptibility increases with decreasing particle size in a systematic way. Our susceptibility value for the NiO reagent powder then corresponds to roughly 100 nanometer particle size. Then Samples D, E, and F have larger particles sizes and Sample C, smaller sizes.

The superparamagnetism of NiO in Sample C is indicated by the enhanced magnetic moment and increased temperature dependence of the moment. However, the detailed dependence differs from that observed in measurements of pure NiO particles.[15] One possible explanation for the temperature dependence observed in Figure 11 may be the presence of a small quantity of very small (10 nanometer) particles in Sample C.

All samples exhibit the presence of paramagnetic "impurities" due to the upturn in magnetic moment below 50 K. A plausible explanation for this upturn is the presence of a small quantity of Ni^{3+} ions in NiO. The black color of reagent NiO is generally attributed to Ni^{3+} ions associated with excess oxygen, and the gray color of the Ca-Ni-K-O samples investigated here may well have this origin as well. The concentration of these presumed Ni^{3+} ions can be estimated based on the magnitude of the low temperature peaks in Figure 11, using Curie's law. It may also be estimated from the curvature in Figure 9, by attributing the curvature to the saturation of the magnetic moment at low temperature and high fields. In either case, the ratio of Ni^{3+} to total nickel is roughly 0.1%.

In summary, the magnetic properties of the Ca-Ni-K-(C-)O mixtures are surprisingly variable. Two of the samples were particularly magnetic, and the plots of magnetic moment were markedly non-linear as functions of the applied magnetic field. These samples contained calcium carbonate. From the magnetic properties alone, elemental ferromagnetic nickel is believed to be present, an expectation which was confirmed by x-ray diffraction. Doping with potassium increased the amount of Ni°. The other four samples had magnetic properties which are attributed entirely to small NiO particles, with susceptibility increasing with decreasing particle size (decreasing calcination

temperature). The sample treated at 485°C was superparamagnetic, with twice the magnetism at low temperatures as NiO reagent. A T^{-1} peak in magnetic moment seen below 50 K in all samples may be due to Ni^{3+} ions.

The presence of nickel metal in NiO samples is readily detected magnetically by the large magnetic moment, large initial susceptibility, and saturation at low applied magnetic fields.

Strontium-Zirconium-Yttrium Oxide Films

Films of strontium-zirconium-yttrium oxide have been fabricated using pulsed laser deposition methods, which provide significant advantages in the preparation of stoichiometric compounds as films and coatings. This process forms novel crystalline film structures and multi-layer, multi-component films at very rapid deposition rates. The technique has simple requirements for the target materials and for the composition and pressure of the surrounding gas environment.

In our study, the Sr-Zr-Y oxide films were prepared on yttria-stabilized zirconia as a buffer film. These buffer films have been shown to lead to better film quality and bonding characteristics in superconducting film applications. The composition of the target used in this studies was $SrZr_{0.9}Y_{0.1}O_{2.95}$. X-Ray diffraction lines corresponding to this composition were observed in the fabricated films. We are presently characterizing in more detail the composition, thickness and morphology of such films. Our initial results suggest that these films are excellent candidates as hydrogen transport membranes in methane activation applications.

Microprobe Results on Ca-Ni-K Oxide Films

Initial studies of Ca-Ni-K oxide films using X-Ray fluorescence microscopy have been conducted at the Advanced Light Source Facility at the Lawrence Berkeley Laboratory. Results show good homogeneity in the films with respect to the Ni and Ca components, with the x-y lateral images consisting of a 125 micron by 125 micron mapping area. Figure 12 shows an image of the Ni distribution in a Ca-Ni-K oxide films. Some regions are indicative of surface particles adhering to the film. Future studies will address the effects of experimental conditions on the film properties and morphology.

V. References

1. P. Pereira, S.H. Lee, G.A. Somorjai, and H. Heinemann, Catal. Lett. **6**, 255 (1990).

2. J. Rasko, P. Pereira, G.A. Somorjai, and H. Heinemann, Catal. Lett. **9**, 395 (1991).

3. J. Rasko, G.A. Somorjai, and H. Heinemann, Appl. Catal. A, General **84**, 57 (1992).

4. D.M. Ginter, E. Magni, G.A. Somorjai, and H. Heinemann, Catal. Lett. **16**, 197 (1992).

5. Y.F. Chang, G.A. Somorjai, and H. Heinemann, J. Catal. **141**, 713 (1993).

6. Y.F. Chang, G.A. Somorjai, and H. Heinemann, J. Catal. **142**, 697 (1993).

7. X.L. Mao, D.L. Perry, and R.E. Russo, J. Mater. Res. **8**, 2400 (1993).

8. C.P. Bean, J. Appl. Phys. **26**, 1381 (1955).

9. I.S. Jacobs and C.P. Bean, in Magnetism, Vol. III, G.T. Rado and H. Suhl, eds., Academic Press 271 (1963).

10. J.I. Gittleman, B. Abeles, and S. Bozowski, Phys. Rev. B **9**, 3891 (1974).

11. T. Furubayashi and I. Nakatani, Solid State Commun. **74**, 821 (1990).

12. W. Gong, H. Li, Z. Zhao, and J. Chen, J. Appl. Phys. **69**, 5119 (1991).

13. A. Mauger, M. Escorne, V. Paul-Boncour, A. Percheron-Guegan, J.C. Achard, and J. Barrault, J. Phys. Chem. **92**, 6004 (1988).

14. M. Escorne, A. Mauger, V. Paul-Boncour, and A. Percheron-Guegan, Solid State Commun. **76**, 757 (1990).

15. J.T. Richardson and W.O. Milligan, Phys. Rev. **102**, 1289 (1956).

16. J.R. Singer, Phys. Rev. **104**, 929 (1956).

17. L. Neel, Compt. Rend. Acad. Sci. **252**, 4075 (1961); **253**, 9, 203, 1286 (1961); **254**, 598 (1962).

18. L. Neel, J. Phys. Soc. Japan **17**, Suppl. B-I, 676 (1962).

19. J. Cohen, K.M. Creer, R. Pauthenet, and K. Srivastava, J. Phys. Soc. Japan **17**, Suppl. B-I, 685 (1962).

20. W.J. Schuele and V.D. Deetscreek, J. Appl. Phys. **33**, 1136 (1962).

21. S. Matsuo, S. Satou, M. Suzuki, M. Sano, and H. Nakano, Z. Phys. D - Atoms, Molecules, Clusters **18**, 281 (1991).

22. J.T. Richardson, D.I. Yiagas, B. Turk, K. Forster, and M.V. Twigg, J. Appl. Phys. **70**, 6977 (1991).

23. J.T. Richardson, B. Turk, M. Lei, and M.V. Twigg, Appl. Catal. **83**, 87 (1992).

24. Ref. 2, Secs. 4 and 5.

Figure Captions

Figure 7. Magnetic moment per unit mass as a function of applied field for two Ca-Ni-O samples at 5 K, with and without potassium doping.

Figure 8. X-ray diffraction data for Samples A and B, showing the presence of small peaks for Ni°.

Figure 9. Magnetic moment per unit mass as a function of applied field for Samples C, D, E, and F, at 5 K.

Figure 10. Magnetic moment of all Ca-Ni-O samples at lower fields, at 5 K.

Figure 11. Magnetic moment vs. temperature for NiO reagent powder and Samples C, D, and F, at 40 kG. Data for NiO were scaled for comparison with the other samples, as discussed in the text. Sample E (not shown) was similar to D and F.

Figure 12. X-Ray Fluorescence Mapping of the Ni component in Ca-Ni-K Oxide films

Table 1: Sample composition as determined from x-ray diffraction.

Sample	Dominant Calcium Phase	Other Calcium Phases	NiO	Ni(o)
A	$CaCO_3$	$CaO, Ca(OH)_2$	Yes	Yes
B	$CaCO_3$	$CaO, Ca(OH)_2$	Yes	Yes
C	$Ca(OH)_2$	—	Yes	No
D	$Ca(OH)_2$	—	Yes	No
E	$Ca(OH)_2$	—	Yes	No
F	$Ca(OH)_2$	—	Yes	No
NiO	—	—	Yes	No

Table 2: Magnetic moment (emu/gm) at 40 kG and 280 K. The second column is normalized to the mass of NiO, computed from sample composition.

Sample	Moment per gm	Moment per gm of NiO
A	0.28	1.23
B	0.74	3.30
C	0.18	0.53
D	0.134	0.41
E	0.134	0.41
F	0.127	0.39
NiO	0.47	0.47

Figure 7. Magnetic moment per unit mass as a function of applied field for two Ca-Ni-O samples at 5 K, with and without potassium doping.

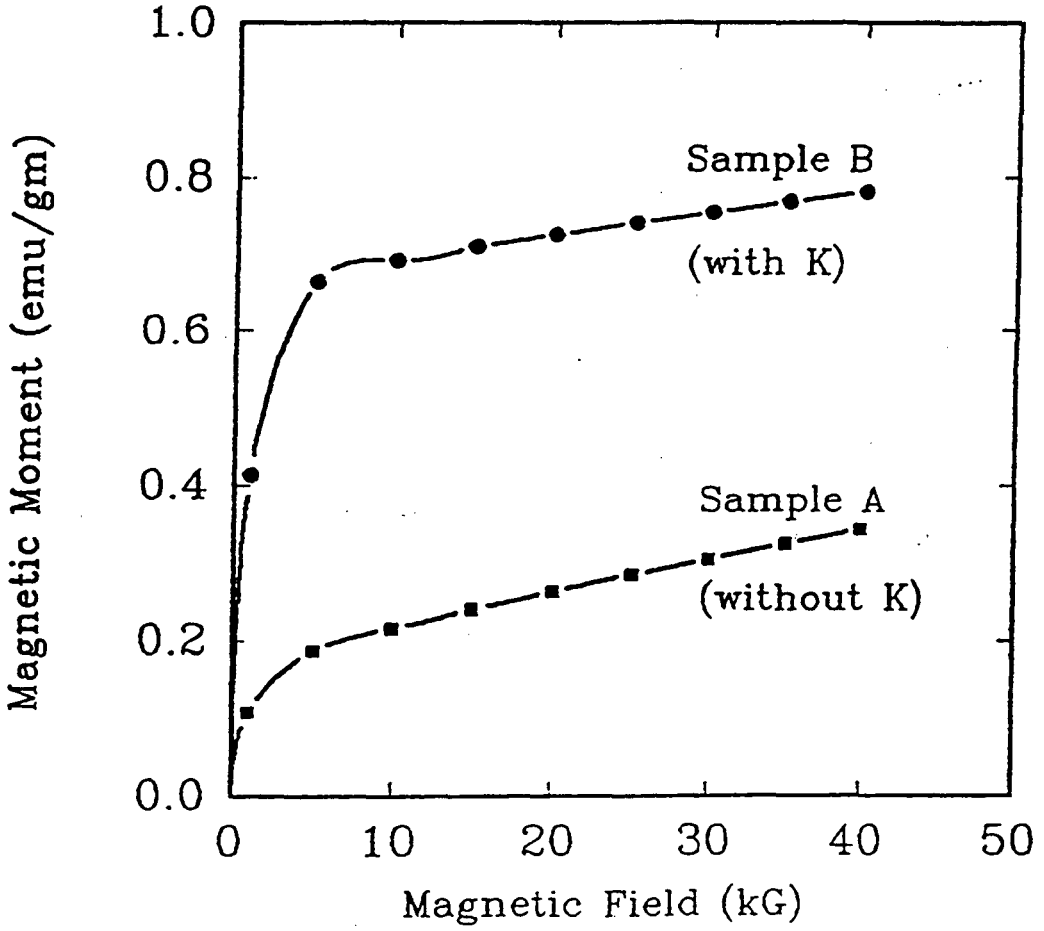

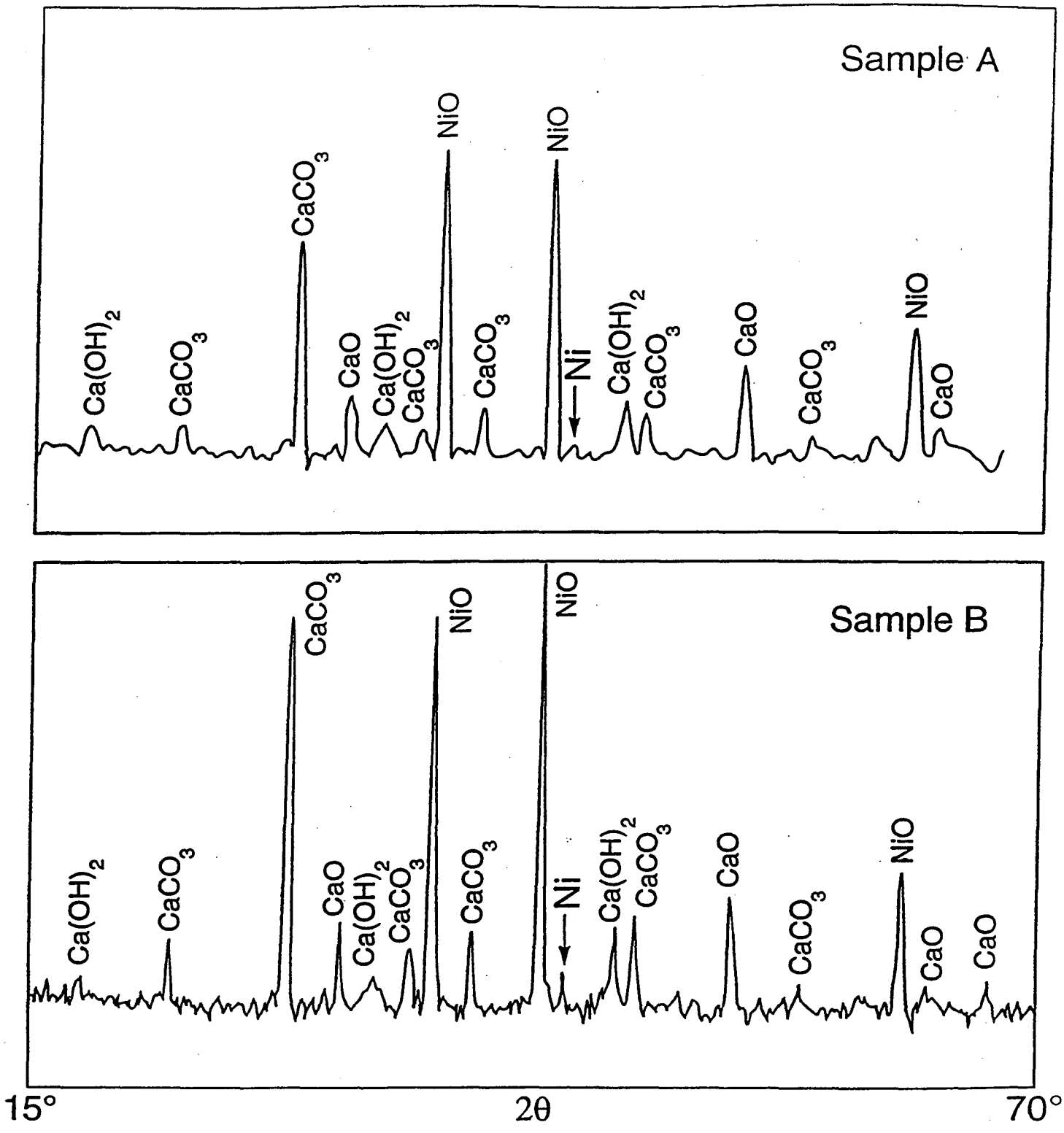

XBL 937-4070

Figure 8. X-ray diffraction data for Samples A and B, showing the presence of small peaks for Ni°.

Figure 9. Magnetic moment per unit mass as a function of applied field for Samples C, D, E, and F, at 5 K.

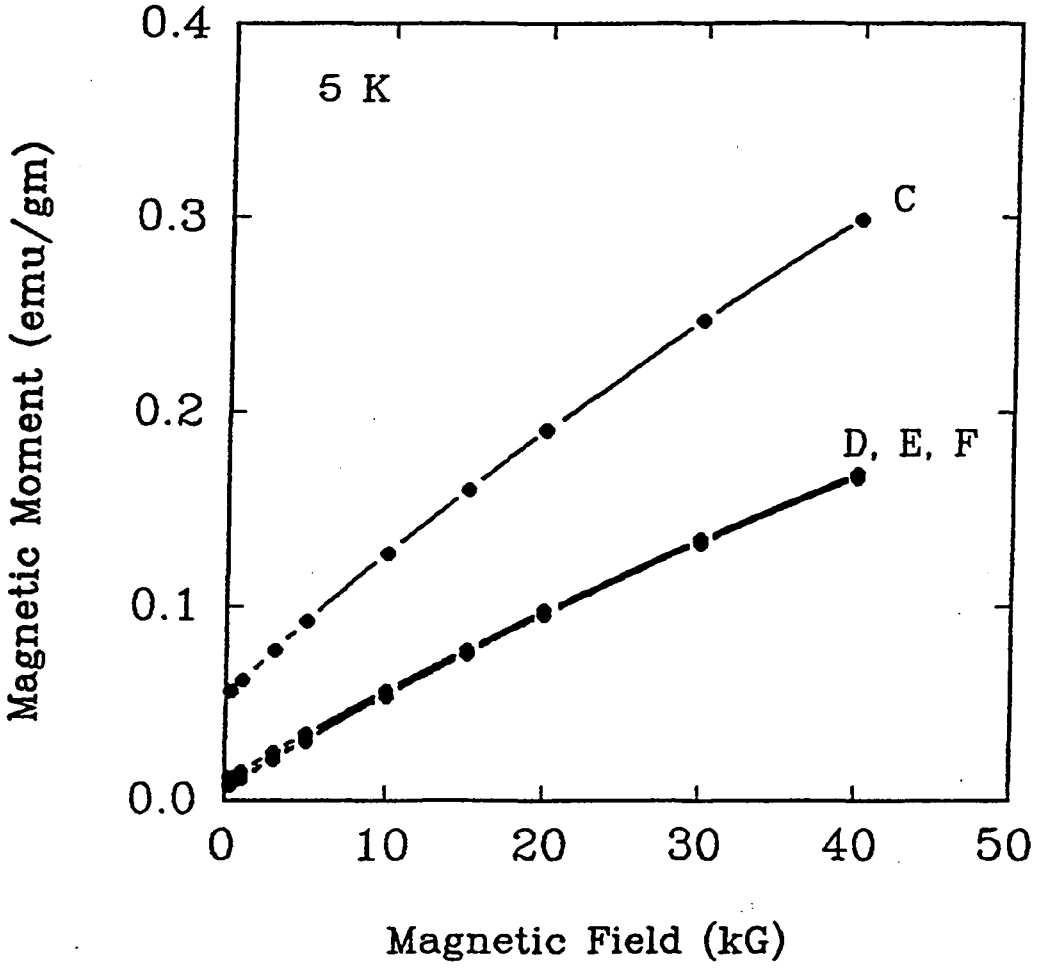

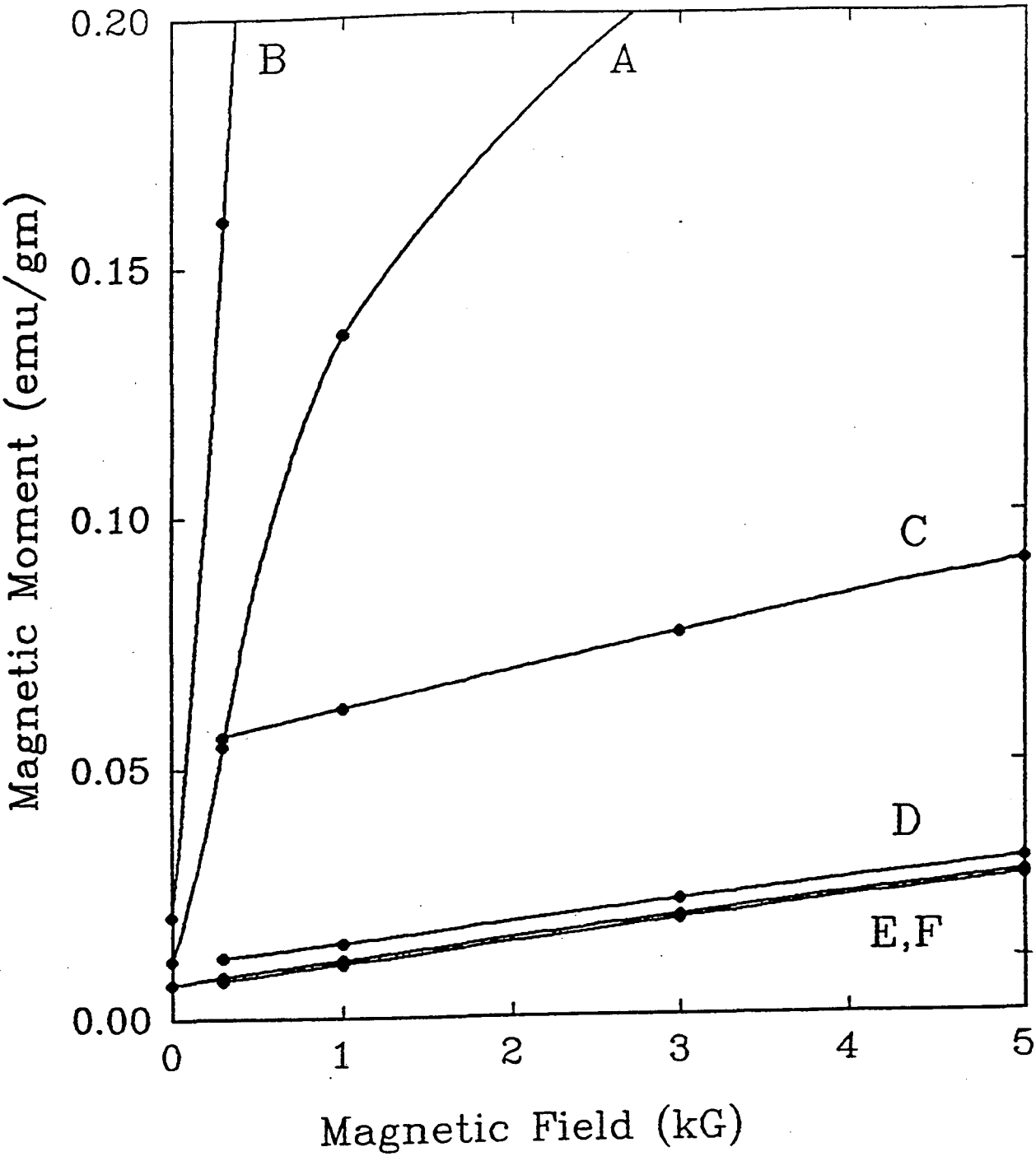

Figure 10. Magnetic moment of all Ca-Ni-O samples at lower fields, at 5 K.

Figure 11. Magnetic moment vs. temperature for NiO reagent powder and Samples C, D, and F, at 40 kG. Data for NiO were scaled for comparison with the other samples, as discussed in the text. Sample E (not shown) was similar to D and F.

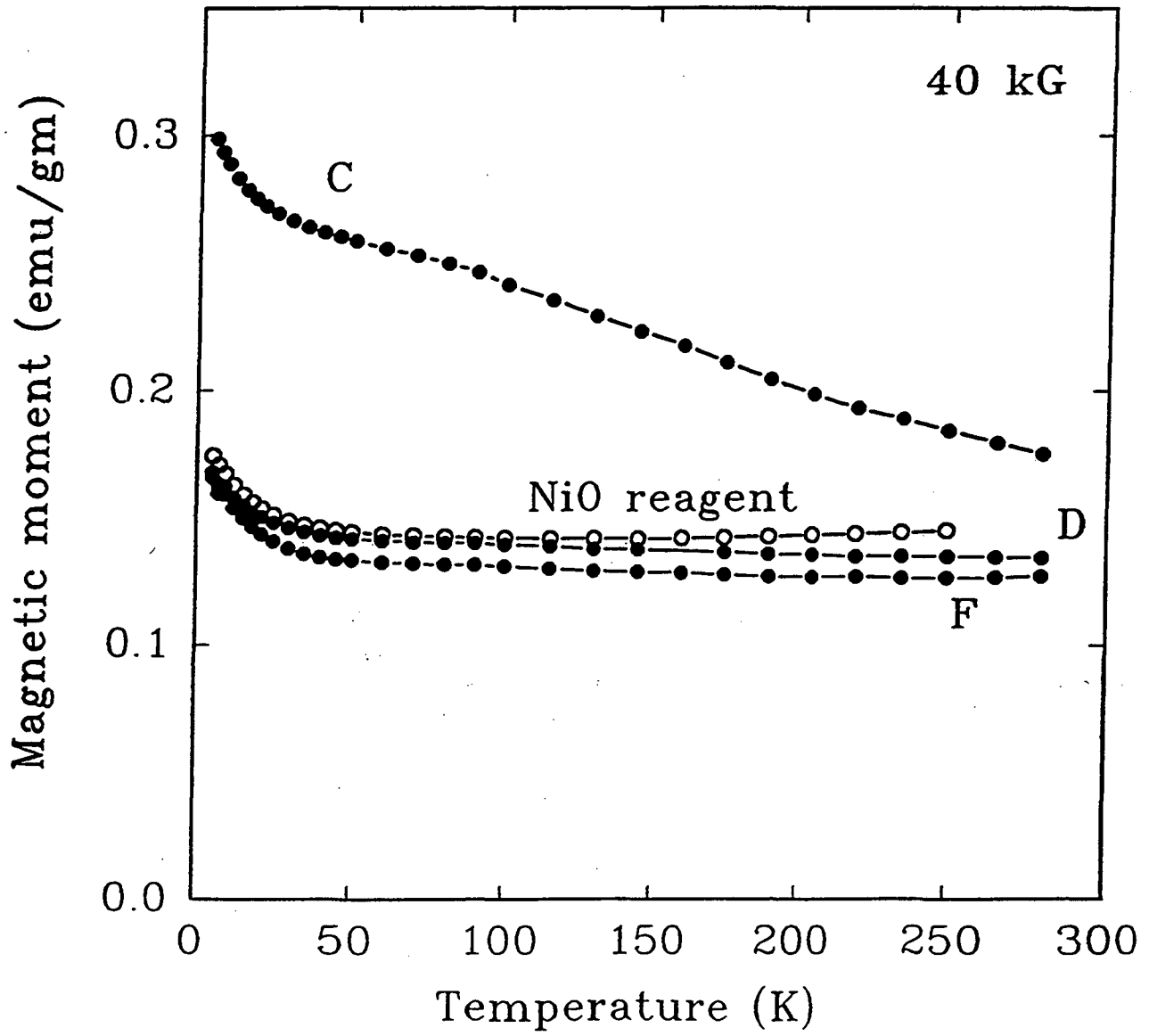

Figure 12. X-Ray Fluorescence Mapping of the Ni component in Ca-Ni-K Oxide films

ATTACHMENT

SLIDES PRESENTED AT THE FOSSIL ENERGY / NATIONAL LABORATORY JOINT MEETING

DULLES AIRPORT, WASHINGTON, D.C.

JUNE 21, 1994

Oxidative Coupling: Literature Data of C_2^+ Selectivity vs. Conversion

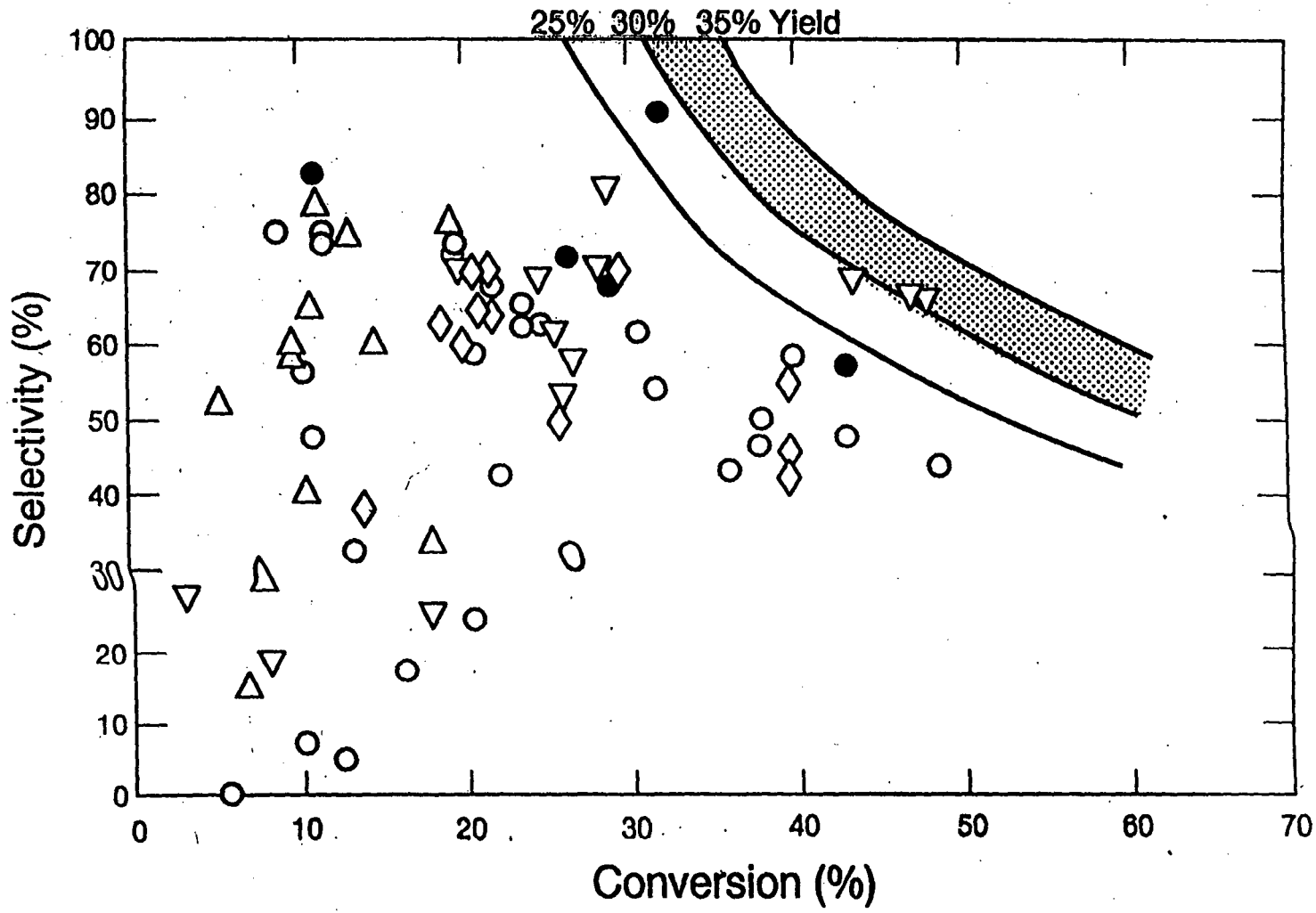

XCG 9011-4548

$$2\ CH_4 + O_2 \rightarrow C_2H_4 + 2\ H_2O$$

Major Findings

- A new catalyst system has been found comprising mixtures of oxides of calcium, nickel and potassium.

  The catalyst system works best in the presence of steam.

  High selectivities in C_2 and hydrocarbons (80+ %) are obtained at ~25% conversion, resulting in ~20% yield of higher hydrocarbons.

  The work has been published and has been taken up by workers in Holland and at LSU.

Oxidative Coupling of Methane to Ethane/Ethylene

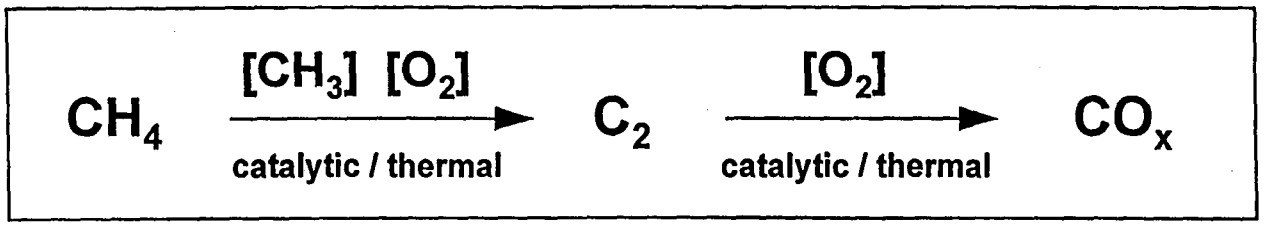

- Homogeneous reaction results in CO, CO_2 formation
- Approaches to overcome C_2 yield limitations:
  - Catalytic methyl radical generation
  - Staged oxygen injection
  - Separate hydrocarbons and oxygen:

    - Hydrogen transport membrane
    - Cyclic methane coupling and hydrogen removal

Use of Hydrogen Transport Materials to Prevent CO_x formation

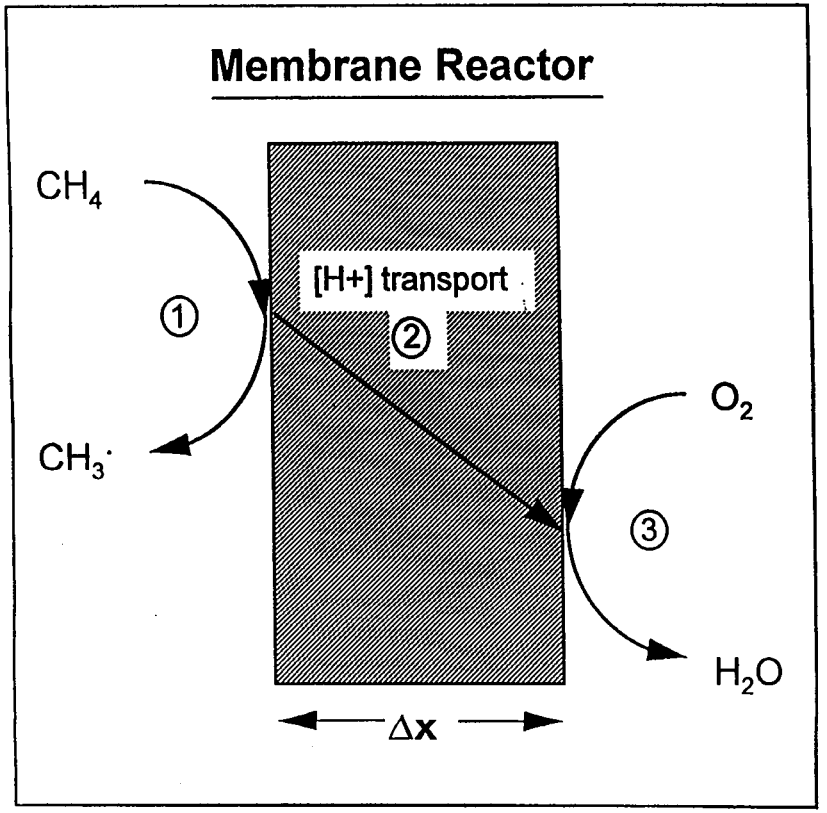

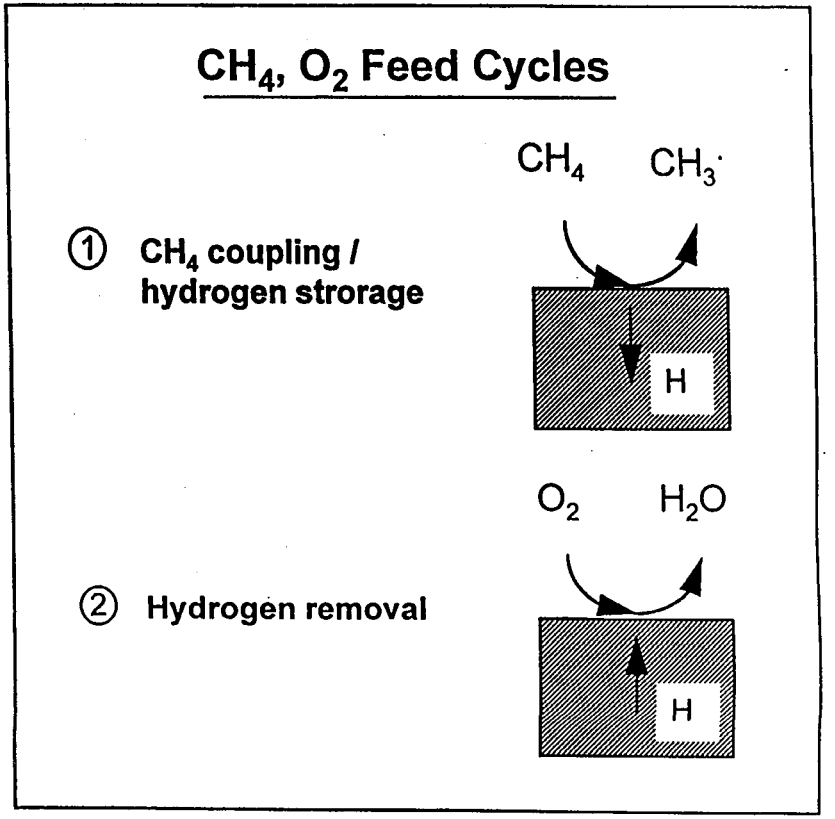

- Perovskites of type $SrM_{0.9}Yb_{0.1}O_{2.95}$ **(M = Ce, Zr)**

- Selective transport of hydrogen at 500 - 900 °C

[Iwahara, et al. Solid State Ionics, **18** & **19** (1986) 1003]

LAWRENCE BERKELEY LABORATORY
CENTER FOR ADVANCED MATERIALS
1 CYCLOTRON ROAD
BERKELEY, CALIFORNIA 94720